Crustal structure and the seismogenic environment in Yunnan imaged by double-difference tomography

Ya Sun[1,2], Shilin Deng[1,2] and Jiwen Huang[1,2]*

[1]Key Laboratory of Metallogenic Prediction of Nonferrous Metals and Geological Environment Monitoring, Ministry of Education, Central South University, Changsha, China, [2]School of Geosciences and Info-Physics, Central South University, Changsha, China

The large-scale faulting and earthquake activities that developed extensively in the Yunnan area are associated with the collision of India and Eurasia. The fine crustal structure can provide a better understanding of the crustal deformation, seismogenic environment, and rupture processes. We performed a new 3-dimensional (3D) P wave velocity structure and seismic relocation using double-difference tomography based on seismic observations. The tomography images show that large-scale low-velocity anomalies spread around the margin of the south Chuan−Dian Block, Xiaojiang fault (XJF), and the Lijiang−Xiaojinhe fault (LJ-XJHF) in the middle and lower crust. There is an obvious high-speed anomaly in the Emeishan large igneous province (ELIP). We infer that the low-velocity anomaly under the LJ-XJHF zone may be derived from the lower crustal flow extruded from the central Tibetan plateau and obstructed by the ELIP, while the velocity anomalies around the XJF might be caused by shear heating, which is associated with the large-deep strike−slip fault and the transmission of stress in the southeast direction. The inversion results also show that the Yangbi earthquake occurred at the NW−SE boundary of high and low velocity from the upper crust to the lower crust, which coincides well with the location of the Yangbi earthquake sequence and the Weixi−Qiaohou fault. Meanwhile, the earthquake relocations show that the aftershocks are mainly distributed at low velocities. All the aforementioned research results indicate that the Yangbi earthquake might be attributed to the intrusion of the soft material flow along the Weixi−Qiaohou fault in the NW−SE direction. These low-viscosity crustal materials would cause brittle fractures and result in NW−SE sinistral strike−slip faults.

1 Introduction

The collision between India and Eurasia and the resistance of the Yangtze plate resulted in a regional high-stress environment and many destructive earthquakes in the Southeast margin of the Tibetan Plateau (SE Tibet) (Xu et al., 2013; Wang and Burchfiel, 2000; Zhang et al., 2004). The northeast extrusion of the Indian continent into the Eurasian continent has led to the vertical thickening of the crust under the Tibetan Plateau, as well as the crustal flow and migration of deep materials. The stress is not only transferred within the plateau but also

transferred to the margin of the plateau, forming a series of Cenozoic structures and landforms, accompanied by seismic activities and environmental evolution (Wang and Burchfiel, 2000; Zhang et al., 2004; Xu et al., 2013). SE Tibet was, therefore, demonstrated to have undergone intense deformation and a sudden thickening of the crust and surface uplift (Figure 1A). Two representative models have been put forward to simulate the process of crustal deformation and the uplift of SE Tibet. The first model is the rigid block extrusion along the large deep fault with coherent deformation of the crust and upper mantle lithosphere (Tapponnier and Molnar, 1976; Tapponnier et al., 1982). The second model is the general model of lower crustal flow (Royden et al., 1997; Clark and Royden, 2000), which considers the lower crust as the weak material channel that led to decoupled deformation of the lithosphere mantle and crust since no substantial stress transfers from the low-viscosity materials. Both models suggest that the material of the Tibetan Plateau has extruded into SE Tibet from the lower crust under the compressive stress of the uplift of the Tibetan Plateau. However, the specific extrusion model has not been confirmed.

Yunnan has bred a series of unique deep fault zones, mainly including the Nujiang fault, Lancang River fault, and XJF in the N–S direction; Red River fault (RRF) in the NW–SE direction; and LJ-XJHF in the NE–SW direction (Zhang et al., 2004). Yunnan is different from the northern Chuan–Dian Block and other steep plateau boundaries. Its terrain is relatively flat, and the surface gradient is small. In the process of surface uplift and crustal thickening, there is no obvious large-scale shortening in the crust in this region (Figure 1). However, the current GPS observation shows that there is a large-scale surface movement in this area, and the plateau materials flow from the southeast edge to the east–southeast direction (Cheng et al., 2012). Although previous studies have provided many different perspectives and helped study the deformation mechanism of the crust in this region, the specific distributions of these lower-velocity anomalies are always heterogeneous (Yao et al., 2006). The existence and distribution of the crustal channel flow have also been questioned by various

scientists in some new studies (Bai et al., 2010; Bao et al., 2020; Dai et al., 2020). Moreover, the relationship between seismic activities and lower crustal flow is also unclear.

On the other hand, in the past 30 years, hundreds of earthquakes with a magnitude above 6.0 have occurred in this area, such as the recent Yangbi earthquake with Ms 6.4 (Long et al., 2021; Zhang et al., 2021) in 2021, the Ludian earthquake with Ms 6.5 in 2014 (Xie et al., 2015), and the Ya'an earthquake with Ms 7.0 (Zhang et al., 2021). It is one of the areas with the strongest crustal deformation and the most frequent seismic activities in China (Xie et al., 2015; Long et al., 2021; Zhang et al., 2021). Most earthquakes occur along the large deep faults and the main tectonic line, such as the RRF, Longmenshan Fault, LJ-XJHF, and XJF. Moreover, the seismogenic mechanism of these earthquakes might be related to the low-velocity region of the crust below the source area, which indicates that the low-velocity region influences the preparation for large earthquakes (Wei et al., 2013; Wei et al., 2019; Wang et al., 2021).

The current stress field state obtained from the GPS observation, combined with the dynamic process of the seismogenic stage, indicates that the earthquake occurrence rate is higher in southwest Yunnan (Kong et al., 2022). The measurement of the stress accumulation of the coseismic, post-earthquake, and inter-earthquake shows that the stress accumulation of the RRF zone, XJF zone, and LJ-XJHF zone is relatively high (Sun et al., 2014; Bao et al., 2020). Recent geophysical studies show that there are two zones of low velocities around the XJF and LJ-XJHF zones (Li et al., 2008; Sun et al., 2014). A GNSS velocity field shows that the XJF zone has a high degree of fault locking and lateral left slip loss rate, which increases the risk of earthquakes (Zhang et al., 2022). Yunnan as the southern part of SE Tibet is the passage zone of the lower crustal material from the center of Tibet to SE Tibet and is an important area to clarify the lithosphere deformation and the seismogenic mechanism for these strong earthquakes. The study of the fine crustal structure and earthquake relocations can reflect available geophysical evidence for the geodynamic model of surface uplift and
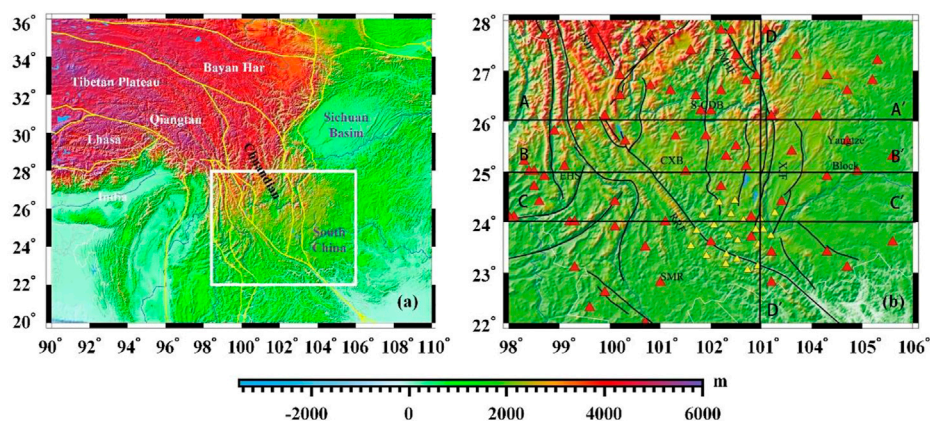

FIGURE 1
(A) Tectonic blocks around the Tibetan plateau. **(B)** Topographic map showing the China Earthquake Administration (CEA) and temporary stations in the southern Chuan–Dian block and its surrounding areas. The red triangle in **(B)** represents the data of the stations of the CEA, and the yellow triangle represents broadband seismic stations installed by Central South University. S-CDB: southern Sichuan–Yunnan block; CXB: Chuxiong Basin; EHS: East Himalayan Block; Yangtze Block: Yangtze plate; SMR: Simao Block; JSJF: Jinshajiang fault zone; LJF: Lijiang fault; ZMHF: Zemuhe fault zone; XJF: Xiaojiang fault zone; RRF: Red River fault zone.

FIGURE 2
Travel time–distance curve of a P wave before selection **(A)** and after selection **(B)**. The data outside the green lines are removed to ensure data quality.

FIGURE 3
Seismic wave ray coverage map; the red triangles represent the data of the CEA, and the yellow triangles represent the data installed by Central South University.
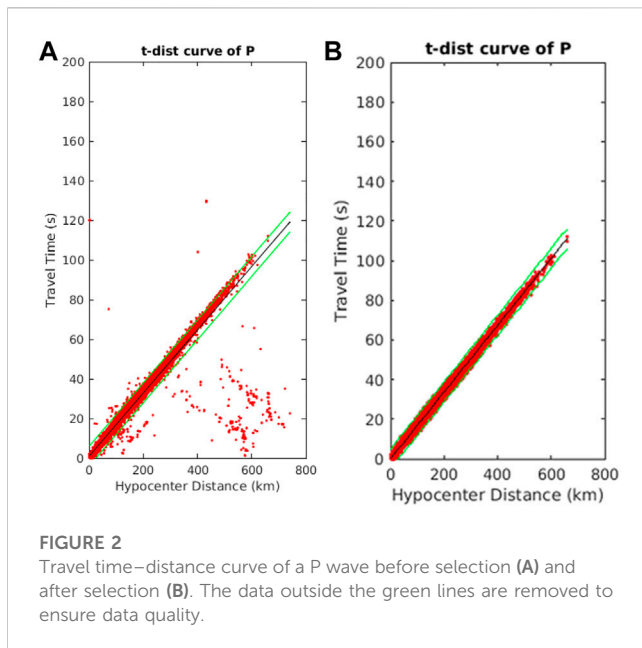
the deep seismogenic environment and mechanism under Yunnan and its surroundings.

Seismic tomography plays an important role in obtaining detailed crustal structure information (Rawlinson et al., 2010; Xin et al., 2019). Many seismic studies have shown and provided valuable geophysical information for the crustal structure and the geodynamic model for surface uplift around SE Tibet (Sun et al., 2012; Lv et al., 2022). However, the distribution of low-velocity anomalies and the relationship between these lower crustal materials and the seismogenic mechanism are still unclear. In this study, we collected a high-quality dataset recorded by the China Earthquake Administration's (CEA) network and a 2-year mobile seismic observation installed by Central South University. We used the collected data to build a new 3D Vp model of the crust of the Yunnan area using the double-difference tomography method (Figure 1B; Waldhauser, 2001; Zhang and Thurber, 2003). The inversion results can give significant information for further understanding the crust structure and the mid-lower crust channel flow and analyzing the deep seismogenic environment and geological structure of the Yangbi area.

2 Data and methods

2.1 Data

We chose 82 seismic stations located in the study region between 98° and 106° in longitude and 22°–28° in latitude recorded by the CEA's network (Zheng et al., 2010) and 22 broadband seismic stations observed for 2 years from 2018 to 2020, which were installed by Central South University. We collected the data of P-wave arrival times from 37,431 earthquakes with magnitudes greater than 1.0 that occurred in Yunnan and its surroundings recorded between January 2009 and December 2020 (https://data.earthquake.cn). Since the first arrival phase was used in the
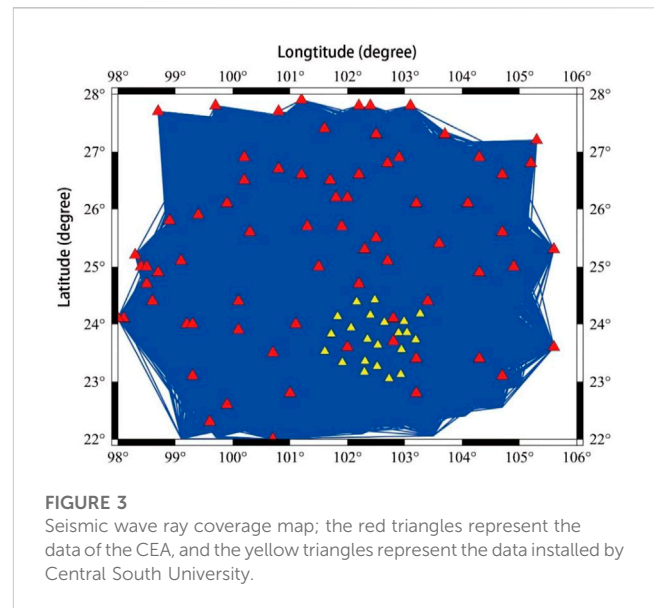
double-difference analysis to invert the crustal structure, we selected the first P-wave arrival time with the smallest travel time and then manually checked the seismograms. The outliers of the P-wave arrival time were further deleted to improve the resolution of the double-difference tomography following two criteria: 1) selecting the phase data with uncertainties smaller than ±9 s, relative to the fitted curve of the major trend of travel time curves for P-wave (Figure 2); 2) the events should be recorded in at least more than eight stations, and the distance between two stations should be larger than 10 km. The number of seismic events was then reduced from 37,431 to 13,590. The number of first P-wave arrivals is 1,743,279. A total of 244,445 differential event pairs were also constructed based on these catalog arrival times. All these P-wave arrivals and the event pairs provide good ray coverage and cross-correlation for reliable double-difference tomography (Figure 3).

2.2 Method

We apply the regional-scale double-difference tomography technique (Zhang and Thurber, 2003) to simultaneously perform seismic tomography and earthquake relocation (Aki and Lee, 1976; Waldhauser and Ellsworth, 2000). Since the travel time between events and stations is calculated in this spherical coordinate system using the finite-difference travel-time algorithm (Aki and Lee, 1976), the double-difference method can produce a more accurate regional-scale seismic velocity structure than the larger-scale seismic velocity structure. Moreover, both the absolute travel time and the relative travel time data are combined to solve the 3D seismic wave velocity of the earthquake source and its surrounding region (Lv et al., 2022).

We first calculate the body-wave travel-time T from an event i to a seismic station k using the ray theory based on the integration along the ray path (Zhang and Thurber, 2003):

$$\tau^i + \int_i^k u\,ds = T_k^i, \tag{1}$$

where $\boldsymbol{u}$ is the slowness, $\boldsymbol{ds}$ is the differential of ray path length, and τ^i is the original time of the event i. Since the relation between the travel time and earthquake event is non-linear, the residual travel-time $\boldsymbol{r}$ can be obtained based on Taylor expansion from Eq. 1. Then, the relation between source parameters and slowness of earthquake event I can be rewritten on each station k:

$$\frac{\partial t_k^i}{\partial \boldsymbol{m}}\Delta \boldsymbol{m}^i + \int_i^k \delta \boldsymbol{u} ds = r_k^i, \tag{2}$$

where $\Delta \boldsymbol{m}^i = (\Delta \mathrm{x}^i, \Delta \mathrm{y}^i, \Delta \mathrm{z}^i, \Delta \tau^i)$ represents the perturbation of source parameters, $\delta \boldsymbol{u}$ is the perturbation of slowness, and $r_k^i = (t^{obs} - t^{cal})_k^i$ is the residual time between the observed differential arrival time and the predicted arrival time, which is the desired perturbation to the hypocenter and velocity structure parameters.

However, the cross-correlation method is used to measure the residual time between different events using the formula $(r_k^i - r_k^j)^{obs}$. We subtract a similar equation for event j measured from station k. The residual time between two events (i and j) at the same station k can be written as follows (Zhang and Thurber, 2003):

$$\frac{\partial t_k^i}{\partial \boldsymbol{m}}\Delta \boldsymbol{m}^i + \int_i^k \delta \boldsymbol{u} ds - \frac{\partial t_k^j}{\partial \boldsymbol{m}}\Delta \boldsymbol{m}^j - \int_j^k \delta \boldsymbol{u} ds = r_k^i - r_k^j, \tag{3}$$

where $\Delta \boldsymbol{m}^{ij} = (\Delta dx^{ij}, \Delta dy^{ij}, \Delta dz^{ij}, \Delta d\tau^{ij})$ is the perturbation of two sources, and the equation can also be simplified as

$$dr_k^{ij} = r_k^i - r_k^j = \left(T_k^i - T_k^j\right)^{obs} - \left(T_k^i - T_k^j\right)^{cal}. \tag{4}$$

dr_k^{ij} is the double difference. $(T_k^i - T_k^j)^{obs}$ is the observed differential travel time between events i and j, and $(T_k^i - T_k^j)^{cal}$ is the calculated differential travel time. When the distance between seismic event pairs is less than the distance between the event and station, the ray path from the earthquake to the station can be approximately regarded as consistent, that is, $\int_i^k \delta \boldsymbol{u} ds = \int_j^k \delta \boldsymbol{u} ds$. Eq. 3 can be written as Eq. 5:

$$\frac{\partial t_k^i}{\partial \boldsymbol{m}}\Delta \boldsymbol{m}^i - \frac{\partial t_k^j}{\partial \boldsymbol{m}}\Delta \boldsymbol{m}^j = r_k^i - r_k^j = dr_k^{ij}. \tag{5}$$

We give an appropriate weight parameter between the differential and the absolute travel time at different stages of inversion (Waldhauser and Ellsworth, 2000).

2.3 Model construction and parameter selection

The inversion formula is obtained by combining the relationship between all seismic event pairs (i, j=1, 2, 3, ..., N) and all the seismic stations (k=1, 2, 3, ...):

$$\boldsymbol{W} \boldsymbol{G} \boldsymbol{m} = \boldsymbol{W} \boldsymbol{d}, \tag{6}$$

where $\boldsymbol{G}$ represents a size of an $M \times 4N$ matrix containing partial derivatives (M is the number of double-difference observations and N is the number of seismic events); $\boldsymbol{d}$ is the data vector; $\boldsymbol{m}$ is the source parameters determined by $\Delta \boldsymbol{m}^i = [\Delta x^i, \Delta y^i, \Delta z^i, \Delta \tau^i]^T$ with a dimension of $4N$; and $\boldsymbol{W}$ is a diagonal matrix weighted for each equation.

The inversion results largely depend on the initial model. Since the crustal structure of the Yunnan area has strong heterogeneity in both vertical and horizontal directions, a one-dimensional initial velocity model cannot invert the accurate result. We then consider the 3D seismic wave velocity model of SWChinaCVM-1.0 observed by the adjoint inversion from body wave and surface wave (Liu et al., 2019; Lv et al., 2022) as the initial model for double-difference tomography in this study (Figure 4). Based on the model resolution and regional seismic ray distribution density, we finally set the node spacing to 0.5° and 1° in our study area and on the edge of the study area, respectively. The vertical grid nodes are set at −5, 0, 1, 5, 10, 15, 20, 25, 30, 35, 40, 50, 60, and 70 km (Figure 5).

To balance the trade-off analysis between data residual variance and model variances, as well as the model smoothness, the L-curve method (Hansen, 1992) is used to obtain the best damping and smoothing factors in inversion. In this study, we choose the best damping factor, 300, and the best smoothing factor, 30 (Figure 6).

2.4 Checkboard test

To estimate the resolution of velocity models and adequacy of the ray path coverage, the checkboard resolution test was used to evaluate the inversion (Zhao et al., 1992). We first add the positive and negative perturbation of 5% to the initial P-wave model and form the input model. The synthetic travel times are then calculated with the same distribution of events and stations as those in real data. The checkboard test is shown in Figure 7, which shows that the velocity anomalies will be well-recovered by travel times from 0 km to 50 km in the study area with good data coverage.

3 Results

3.1 Earthquake distribution after relocation

The seismic event distribution after the relocation is generally consistent with that before relocation. However, the number of seismic relocations is reduced from 23,299 to 19,558. The main reason is attributed to the few data on the arrival time of some seismic events in the inversion process and the lack of good coverage for seismic stations, which lead to the depth of earthquake relocation exceeding the set elevation and locate in the air layer. At the same time, we have deleted the residuals of travel time that are greater than the standard deviation in the inversion. The aforementioned two issues will reduce the number of relocated earthquake events. Moreover, the P-wave residual misfit after the inversion has a smaller range than that before the inversion (Figure 8). The residuals after inversion are concentrated between −2 and 2 s, indicating that the final velocity model is better than the initial model in fitting the actual observation time.

We have drawn the distribution of seismic earthquakes in the horizontal and vertical directions (Figure 9). Vertical cross images along the longitude and latitude after inversion (Figures 9C, D) show that the earthquakes are mainly distributed in the depth of 0–20 km, with less or even no events below 20 km. It also shows that the earthquakes mainly spread in a strip shape in the vertical direction. It indicates that the relocated earthquakes (Figures 9C, D) are more accurate in the vertical direction than those before relocation
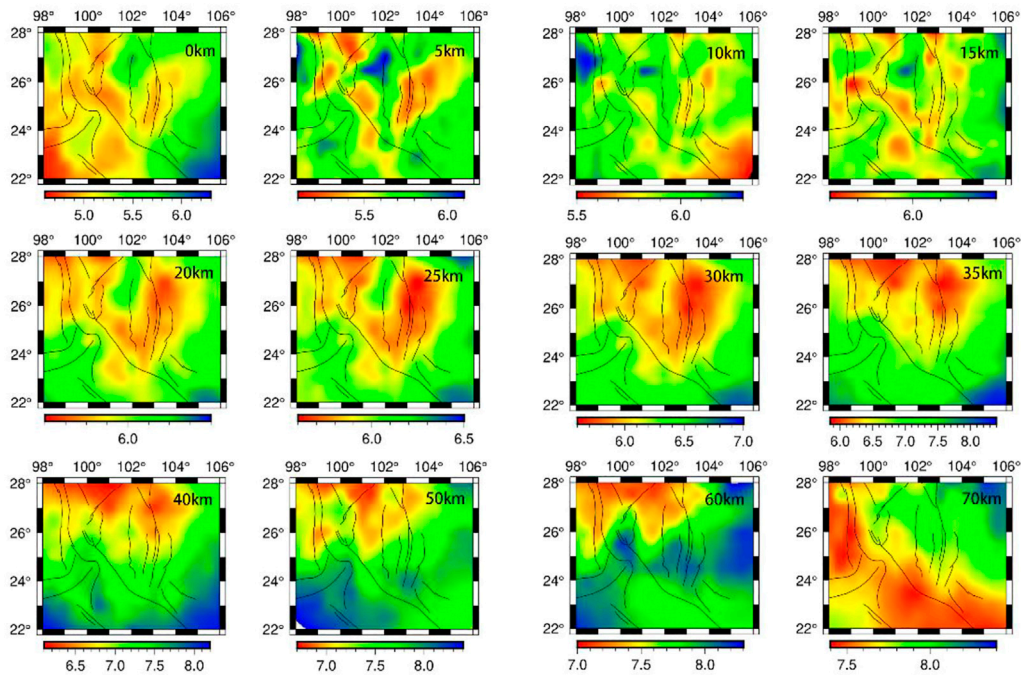
FIGURE 4
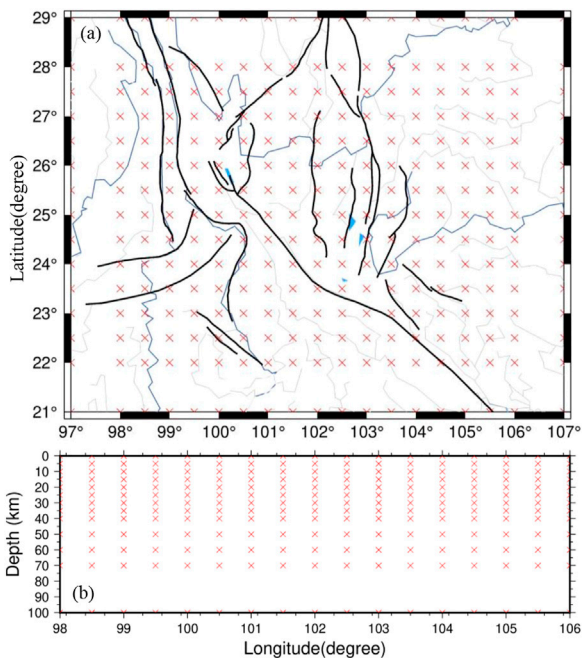3D initial velocity model referred to Lv et al. (2022) and Liu et al. (2019).

FIGURE 5
3D mesh grid for horizontal **(A)** and E−W vertical cross-section **(B)**.
Red crosses represent grid nodes in both horizontal and vertical sections.

(Figures 9B, E). The number of relocated earthquakes in the shallow depth (0–5 km) increases significantly, relative to that before earthquake relocation (Figure 10). Comparing earthquake locations

after inversion and before inversion, we found that the relocated earthquake events mainly spread around the fault zone, especially at the south end of the XJHF, XJF zone, and the north section of the RRF zone (Figure 9A).

3.2 Velocity anomalies

The horizontal slices of the 3D Vp models in the depths of 5, 10, 15, 20, 25, 35, 40, and 50 km are shown in Figure 11, which suggest strong lateral heterogeneities in the crust. The vertical profiles of the Vp images along the four lines (AA', BB', CC', and DD') are shown in Figure 12. At shallow depths of 0–15 km, Vp images show that the low-velocity anomaly is widely distributed around the LJ-XJHF, northern RRF, and Zemuhe fault. Meanwhile, the distribution of anomalies is relatively scattered. It indicates that the velocity anomaly area is largely associated with the geological structure at the shallow depth. For the depth of 15–35 km, the extensive low-velocity anomalies extend to the southwest along the LJ-XJHF zone with a belt shape, while the low-velocity anomaly zone along the XJF also appears on the western margin of the Yangtze Craton, which is consistent with the three-dimensional S-wave inversion (Long et al., 2021). We also found that the high-velocity anomalies extend from the surface to 30 km near the center of the southern Chuan–Dian block, which is consistent with the location of the Emeishan large igneous province. For a depth of 20–35 km, our inversion also shows that the high-velocity anomalies are distributed in the Simao Block and Baoshan Block. The vertical image of 103°E shows that the low-velocity anomalies mainly spread in the longitude of 102–105°E (Figures 12AA'–CC') within the depth of 15–35 km (Figure 12DD'), and this low-velocity
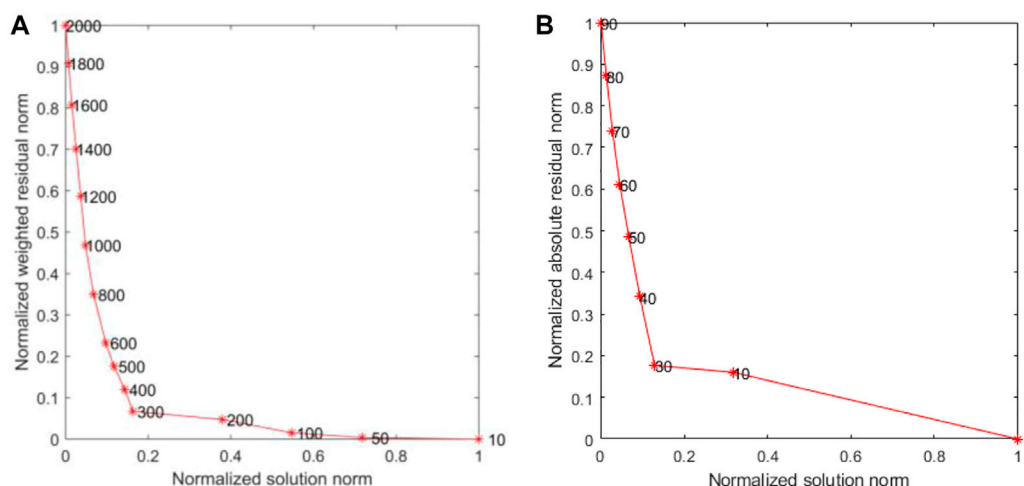
FIGURE 6
L-curve curve, damping factor curve **(A)** and smoothing factor curve **(B)**.

anomaly is continuous from the Zemuhe fault to the intersection of the XJF and RRF. For the vertical seismic profiles of 26 and 25°N, a significant high-velocity anomaly is located around the center of the southern Chuan–Dian block at about 102°E, which separates the low-velocity region into two parts (Figure 12BB'). The vertical P-wave seismic profiles along 26°N, 25°N, 24° N, and 103°E also show that there are obvious low-velocity anomalies in the middle and lower crusts of the XJF and the RRF zones and relatively high-velocity anomalies in the central region of the Chuan–Dian block (Figure 12).

4 Discussion

4.1 Lower crustal flow

Previous studies have generally found that the obvious low-velocity anomalies are widely spread in SE Tibet, especially under the surface of the Chuan-Dian Block (Wei et al., 2013; Bao et al., 2015; Yang et al., 2020). However, the distribution and connection of the low-velocity anomalies in the subsurface, as well as the geodynamics of their deformation, are still unclear.

The horizontal images of the seismic velocity (Figure 11) show a large distribution of low-velocity anomalies at 15–35 km depth below the XJF, LJ-XJHF, and northern RRF zones. The 25-km depth slicing map shows that the low-velocity anomaly is a north–south strip under the Zemuhe fault zone, while it rotates to the southwest along the LJ-XJHF and northern RRF. The distributions of two significant low-Vp anomalies are generally in good agreement with previous research results, including the surface wave tomography (Yao et al., 2010; Bao et al., 2015; Lun et al., 2023) and body wave images (Huang et al., 2019; Deng et al., 2020). Lv et al. (2022) also showed two low-Vp anomaly belts in our study area based on double-difference tomography. The western one distributes from the northwest of the Chuan–Dian block to the LJ-XJH fault and the north part of the RRF, another low-velocity zone around the
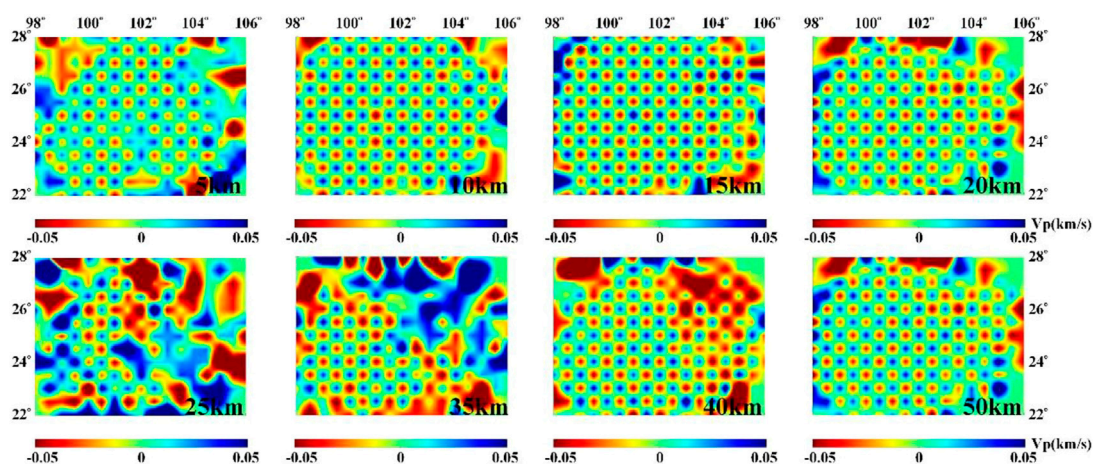

FIGURE 7
Checkboard test for P-wave velocity anomalies at depths of 5, 10, 15,20, 25, 35, 40, and 50 km, respectively.
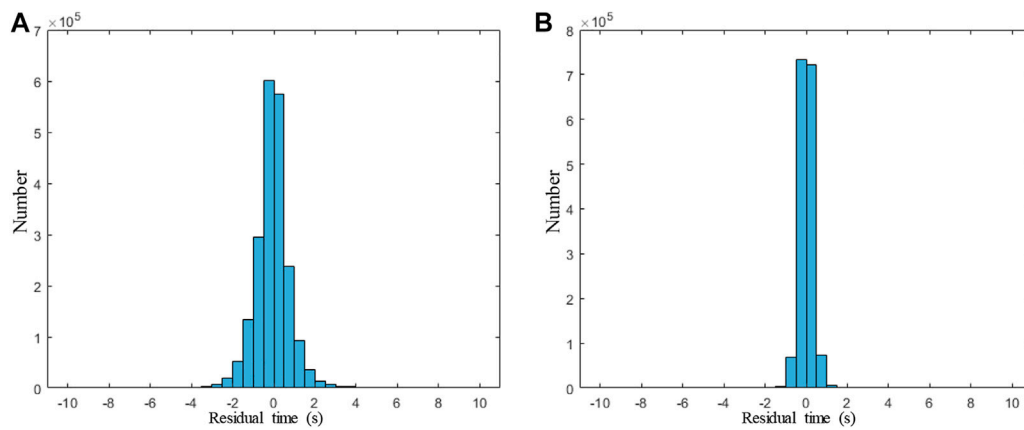
FIGURE 8
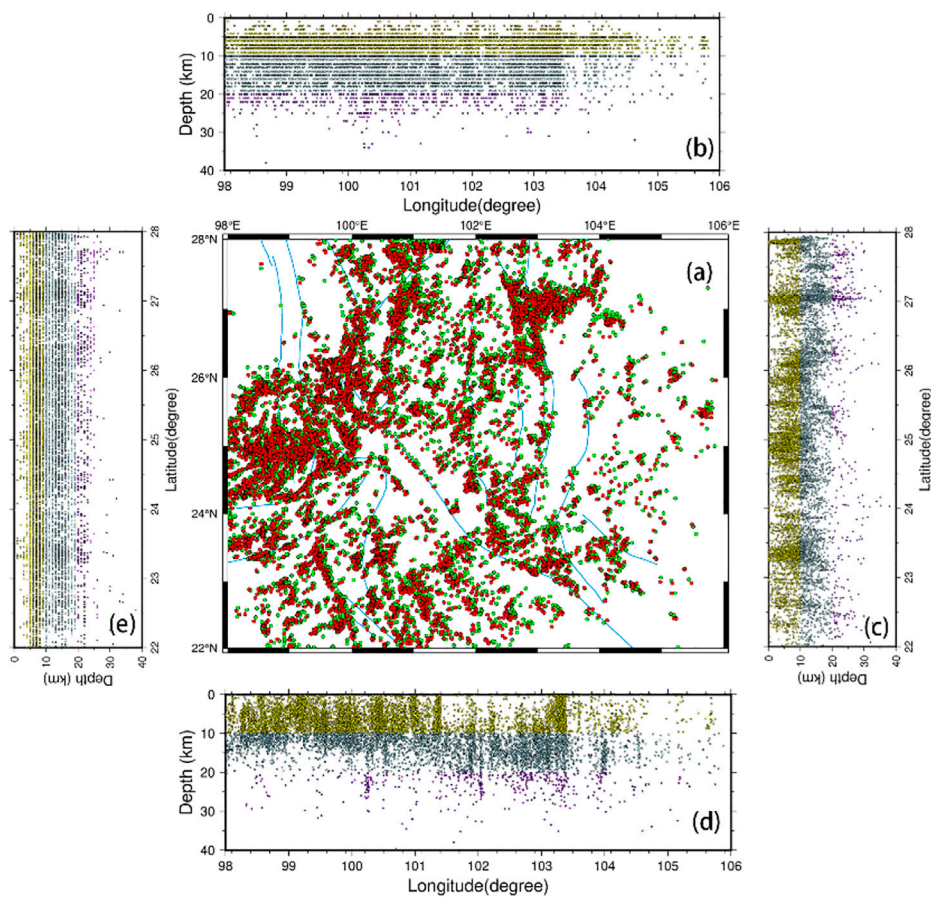Histogram of travel time residuals before **(A)** and after **(B)** relocation for the P-wave.

FIGURE 9
Distribution of seismic events in the horizontal profile **(A)**, **(B)** and **(E)** represent seismic events along the longitude and latitude profiles before inversion, respectively. **(C)** and **(D)** represent the relocation of seismic events along the longitude and latitude profiles after inversion, respectively. Red and green dots in **(A)** represent earthquake locations before and after inversion, respectively. Yellow dots represent earthquake locations in the range of 0−10 km, blue dots represent earthquakes in the range of 10−20 km, and purple dots represent earthquakes below 20 km.
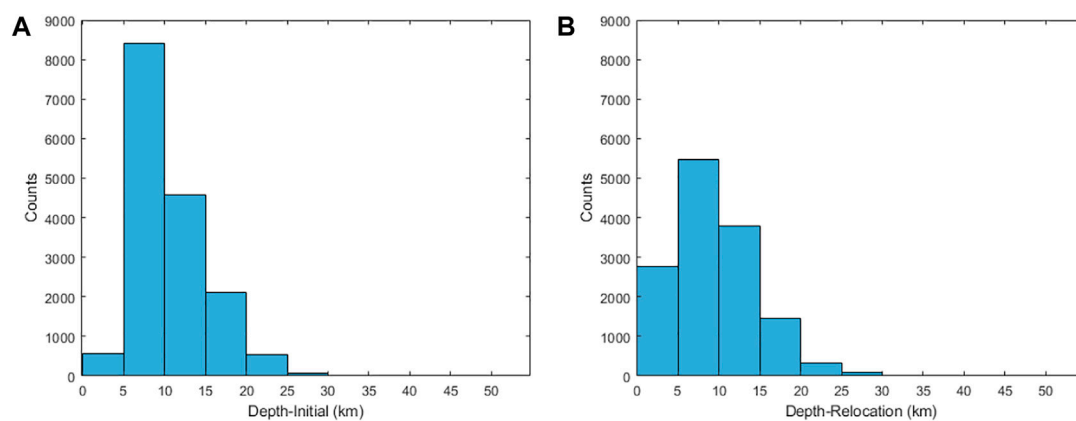
FIGURE 10
Distribution of seismic events in the depth before inversion **(A)** and after inversion **(B)**.

XJF, which are consistent with our results that show significant low velocity at the middle and lower crust in this region. However, the depths of these low-velocity anomalies in this study are 15–35 km, which is relatively less compared to that (20–35 km) found in Lv et al. (2022) and Deng et al. (2020), but similar to that (15–30 km) found in Yang et al. (2020) and Zhang et al. (2020) in the shallow depth. As we know, different data types yield different constraints on the velocity structure. We attribute this difference to the seismic stations that we added, 22 permanent stations around the intersection of the XJF and RRF, which provide good seismic ray coverage and improve the resolution of this area.

Magnetotelluric results (Bai et al., 2010) also show that there are two high-conductivity and low-resistance channels at a depth of 20–40 km. One distributes along the eastern Himalayan syntaxis

(EHS) and the other spreads along the Xianshuihe fault zone and XJF zone, which are consistent with the low-velocity zone below the XJF zone in this study. Geochemical data show that the high conductivity of the crust may be caused by thermal, soft material fluid, and partial melting (Liu et al., 2020). Geothermal data (Hedlund et al., 2012) show that the heat flow value in this region reaches 110 mW/m^2, which is far more than the average value of 61 mW/m^2 in Mainland China. The crustal Q-value images (Zhou et al., 2009) also show the low Q-value located near the XJF zone and LJ-XJHF zone. The low Q-value reflects the high attenuation property of the medium in this area, indicating the inelastic property and soft medium associated with temperature change. Seismic wave anisotropy (Sun et al., 2012) shows that the fast wave direction of Ps splitting near the XJF zone is approximate to the N–S direction, indicating that the material
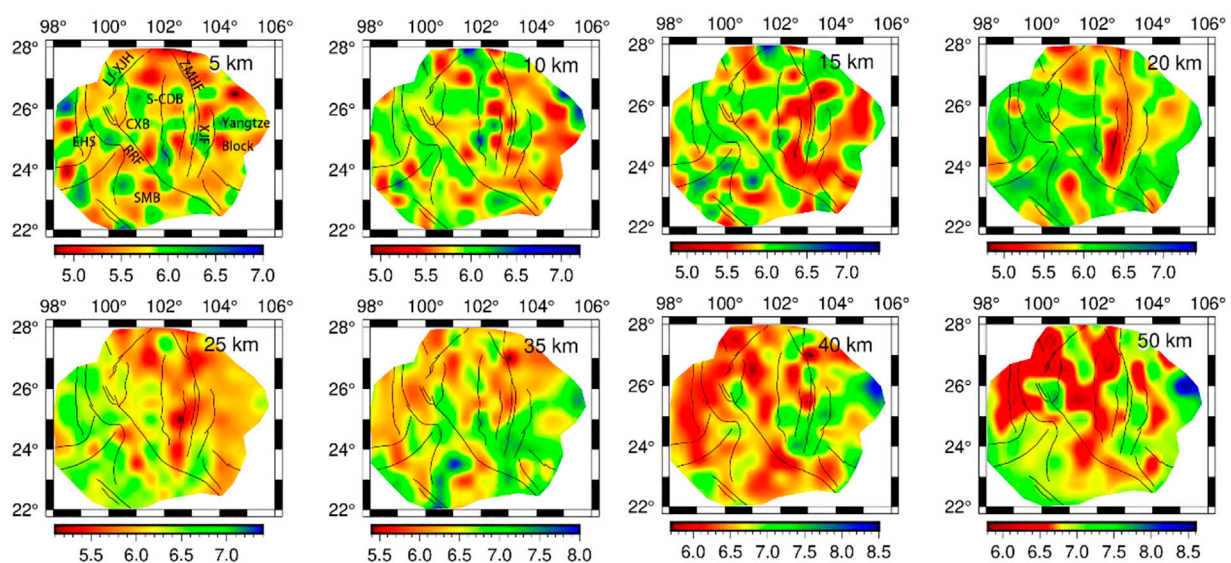

FIGURE 11
Depth slices of P-wave velocity. SMB: Simao Block; S-CDB: South Chuan−Dian Block; RRF: Red River fault; XJF: Xiaojiang fault; ZMHF: Zemuhe fault; LJ-XJHF: Lijiang−Xiaojinhe fault; EHS: East Himalayan Block; SMR: Simao Block; CXB: Chuxiong Basin.
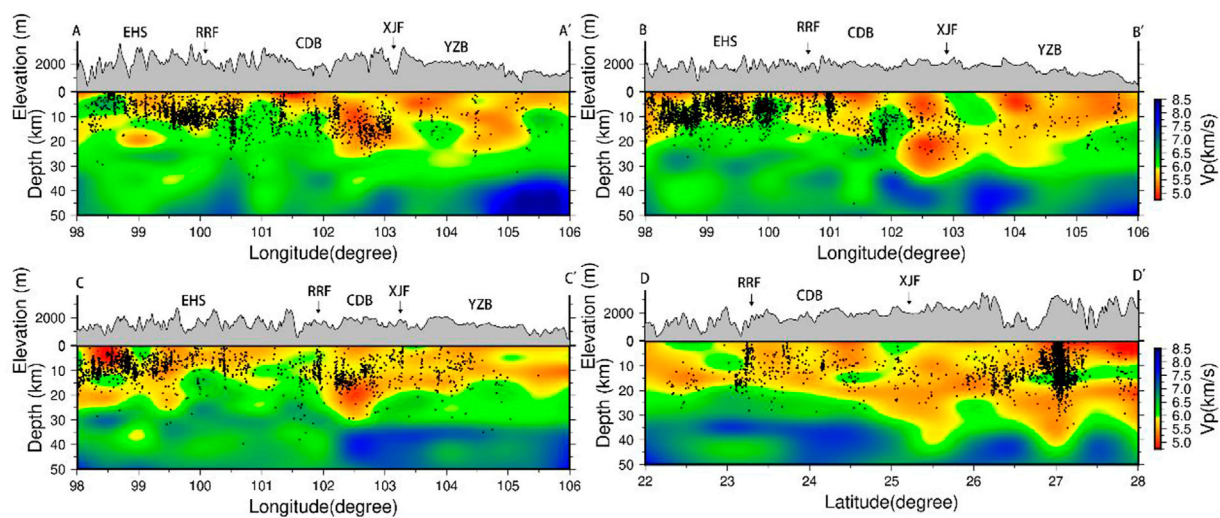
FIGURE 12
P-wave velocity profiles along the latitude of 26°N, 25°N, and 24°N and longitude of 103°E along the **(AA', BB', CC', and DD')** shown in Figure 1B. CDB: Chuan–Dian Block; RRF: Red River fault; XJF: Xiaojiang fault; YZB: Yangzi Block; EHS: Eastern Himalayan syntaxis. Block dots represent the earthquake relocations.

flow direction is approximately in the N–S direction, while it is in the SW direction near the LJ-XJHF zone, suggesting that the material flow direction is near to southwest direction. The aforementioned results are consistent with those of the low-velocity anomaly distribution area in this paper, inferring that the low-velocity anomaly material under the XJF and LJ-XJHF zones may be the crustal flow from the Tibetan Plateau. However, the inversion results show that the low-velocity anomaly is not widely distributed in the southeast margin of the Tibetan Plateau, mainly distributed along the XJF, LJ-XJHF, and north RRF zone.

P-wave velocity images show a relatively higher-velocity region between two low-velocity regions, which is consistent with the location of the ELIP. It is a volcanic province recognized by the international academic community in China, which is widely distributed in Yunnan, Guizhou, and Sichuan provinces (He et al., 2003). At present, it is generally believed that a large-scale eruption of Emeishan basalt occurred in the center of the Chuan–Dian Block during the late Paleozoic at 256–259 Ma. The analysis of the temporal and spatial distribution of basalt and the geochemical properties of the original magma show that the center of the mantle plume is located west of the Emeishan area (Ma et al., 1993; Xu and Zhong, 2001). The study of peridotite phenocrysts and intrusive bodies confirmed the high magnesium content (MgO>16%) of the original magma in the ELIP (Xu and Zhong, 2001). The seismic exploration profiles (Chen et al., 2022) indicate that the mafic and ultramafic rocks have high P-wave velocities. Then, the high Vp velocity might relate to the intrusion of basic and ultrabasic mantle source materials formed by the activity of mantle plumes into the crust during the Permian period. The lower crustal flow would be blocked by this ultrabasic mantle source material when it extrudes from the north of the Chuan-Dian block to the south, resulting in the lower crustal flow converging near the relatively weak region, such as the XJF and LJ-XJHF and the north RRF.

SE Tibet has always been a seismically active region, with destructive earthquakes having occurred here frequently in recent years. Figure 12 shows that a large number of earthquakes are distributed in the middle–upper crust, and the location of earthquakes has a good relationship with the major faults, especially near the boundary of high- and low-velocity anomalies around the XJF and LJ-XJHF zones (Figure 12). This good relation suggests that the mechanical properties of these regions are weak, and there may be a flow of lower crustal material (Clark and Royden, 2000). Our results are also consistent with those of previous studies that show that the Ludian Ms 6.5 earthquake (Xie et al., 2015) and the 2008 Wenchuan Ms 8.0 earthquake (Lei and Zhao, 2009), and the Changning Ms 6.0 earthquake (Lv et al., 2022) occurred in the boundary of high- and low-velocity anomalies. The good correspondence of the aforementioned characteristics indicates that the large deep fault has a significant effect on the regional seismicity and tectonic evolution process.

4.2 Yangbi earthquake

The Yangbi earthquake occurred on the NW-trending Weixi–Qiaohou fault in 2021 with a magnitude of Ms 6.4 (Long et al., 2021; Lv et al., 2022). The Weixi–Qiaohou fault is located on the western part of the RRF, with dextral strike–slip movement and obvious seismic activity on the Weixi–Qiaohou fault since the Late Quaternary (Sun et al., 2022). Meanwhile, the Weihe–Qiaohou fault has controlled the Weishan Quaternary Basin. Due to the collision between the Indian and Eurasian plateaus and obstruction by the Yangtze Craton, this area has suffered eastward extrusion of the Tibetan Plateau and compression in the east and west directions (Wang et al., 2017). In addition, the Chuan–Dian Block is the junction of the Indian plate subducting to the Burmese plate, and
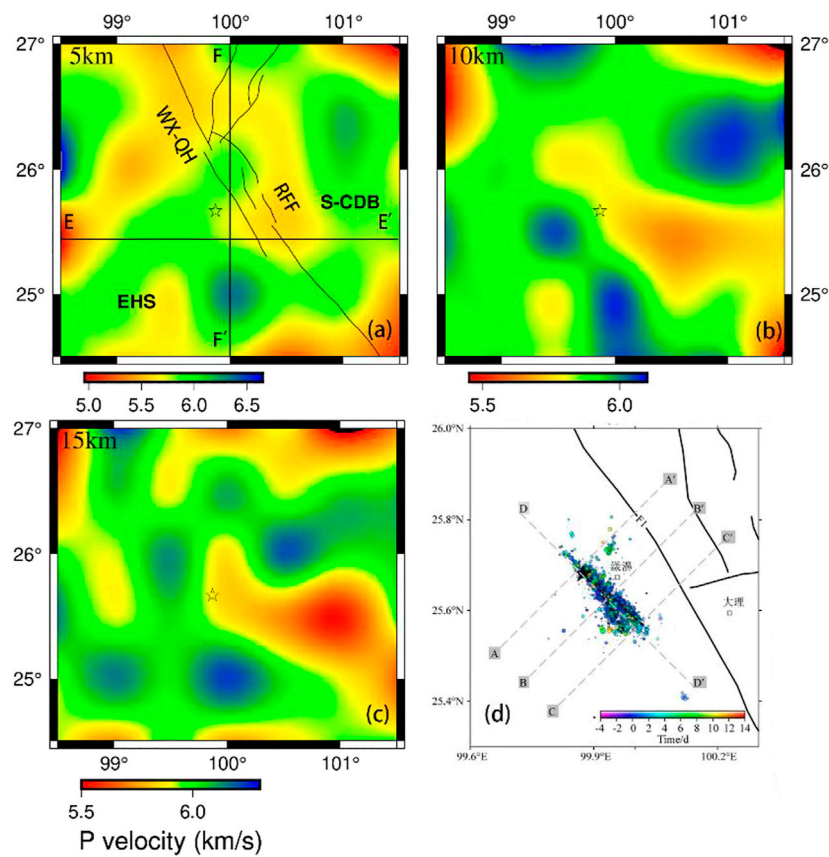
FIGURE 13
Horizontal slice of P-wave velocity and earthquake sequence diagram in the Yangbi earthquake area. **(A–C)** represent the P wave velocity at depth of 5, 10, and 15 km, respectively. The star indicates the location of the Yangbi earthquake. WX-QHF: Weixi–Qiaohou fault; RRF: Red River fault zone. The figure in the lower right region is the earthquake sequence map. **(D)** Referred by Hu et al. (2021)
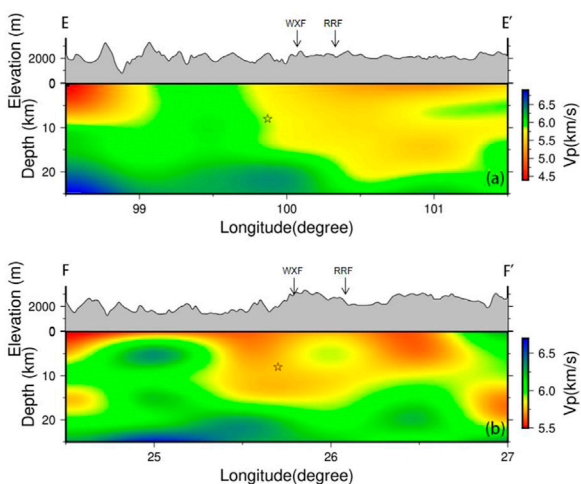

FIGURE 14
P-wave velocity vertical profiles across the Yangbi earthquake with 25 km depth along the EE' and FF' in Figure 13A, which is zoomed in from Figure 11. **(A,B)** represent the profiles of EE' and FF'. The star indicates the location of the Yangbi earthquake. WXF: Weixi fault; RRF: Red River fault zone.

a large-scale fault and extreme seismic activities have developed in this area (Hu et al., 2021).

We enlarged the seismic wave velocity structure in the Yangbi area and drew the three layers and two vertical cross profiles of P-wave velocity (Figures 13A–C, 14A, B). Our results show that there is a clear high- and low-velocity boundary in the Yangbi area, and the velocity anomaly distributes in the NW–SE direction at a depth of 5–15 km (Figures 13A–C, 14). With the increase in depth, the low-velocity anomaly extends to the southeast. Figure 13 shows that the center of the Yangbi earthquake is located in the boundary of high- and low-Vp anomalies, which is consistent with the result of Lv et al. (2022) and Hu et al. (2021). The relocation of the Ms 6.4 Yangbi earthquake sequence shows that the sequence is about 3–13 km away from the nearest known Weixi–Qiaohou fault (Figure 13D), (Li et al., 2022; Lu et al., 2022), indicating that the Yangbi earthquake occurred in the shallow area of the upper crust (Long et al., 2021). Meanwhile, the stress transmitted into the surrounding tectonics caused by the Yangbi earthquake affects the magnitude of Coulomb stress in the southeastern section of the Weixi–Qiaohou fault, significantly increasing the stress in this fracture zone.

The relocation of the earthquake sequence also suggests that the aftershocks of the main earthquake along the northwest segment of the

Weixi–Qiaohou fault are relatively shallow and dense, while those in the southeast part are deeper and dispersed. The seismic cross-sections from the main shock and layer profiles (Figure 14) show that the P-wave low-velocity anomalies extend SE in the deep region and NW in the shallow region. The domain tectonic stress field observed from the focal mechanism solution of the earthquake sequence shows that the seismogenic structure is an NW–SE-trending right-lateral strike–slip movement near the horizontal principal compressive stress. The dislocation type of the main seismogenic fault is generally consistent with that of the Weixi–Qiaohou fault. In addition, the direction of the regional tectonic stress field in the northern segment of the RRF is mainly NNW–SSE (Long et al., 2021). The obvious low-Vp anomalies were distributed around the northern part of the RRF in the upper crust with a depth of 0–15 km, which was interpreted as the weak material flow. The recent ambient noise tomography shows that the lower crustal flow is divided into two ranges in the southern Chuan–Dian block, one along the XJF and the other extending from the LJ-XJHF to the RRF (Liu et al., 2019). Due to the southeast extrusion along the RRF and the clockwise rotation of the southwest Chuan–Dian Block (Long et al., 2021), the extension stress may continue to be transferred southeast along the RRF.

Moreover, the inversion of the b-value shows that the main Yangbi earthquake occurred near the peak values of tidal body strain and Coulomb stress (Hu et al., 2021; Li et al., 2022; Zhang et al., 2022), which reflects the seismic activity of the Yangbi earthquake might be affected by fluid migration (Sun et al., 2022). The high-resolution seismic images of the Yangbi earthquake sequence based on deep learning suggest that a long and narrow strip structure around this area can be analyzed as a channel for material fluid migration (Jin et al., 2019). Geothermal data for regions near the Yangbi earthquake area show that a large number of medium–higher heat flows distribute on the Red River and Weishan–Qiaohou faults (Hu et al., 2000). The observed large low-velocity anomalies around the west of the Yangbi earthquake source have a good correspondence with the low Poisson's ratio and high heat flow (Hu et al., 2000; Liu et al., 2021). The coincidence of these observations implies that the crust here is relatively weak, which might represent the crustal material flow. The studies of earthquake sequences and seismic wave images show that most continual earthquakes occur at the boundary of high- and low-velocity regions (Huang and Zhao, 2004; Mooney et al., 2012), where the large stress and strain energies are easily accumulated (Yang et al., 2021). Combined with the stress, earthquake sequence distribution, and geothermal activity, we infer that cracks were caused by the main Yangbi earthquake around the fault zone. Due to the extrusion of middle and lower crustal flow upwelling along these cracks, the crustal flow further accelerated the fracture of the cracks, resulting in a series of aftershocks.

5 Conclusion

In this study, we construct 3D P-wave velocity images and seismic relocation in the Yunnan region (22˚–28˚N, 98˚–106˚E) using the double-difference tomography method, based on the P-wave travel time data recorded by 82 seismic stations in the region from 1 January 2009 to 31 December 2020, and 22 temporary stations installed by Central South University from 2018 to 2020. These results provide some new geophysical evidence for the seismogenic environments of regional earthquakes and the crustal deformation under Yunnan and its surroundings.

(1) The seismic images show that there are two obvious low-velocity zones at a depth of 15–35 km. The east belt distributes along the XJF in the N–S direction, while the west belt extrudes from the LJ-XJHF and rotates to the north RRF. These observations have good correspondence with the high Vp ratio, significant crustal anisotropy, and high heat flow. The coincidence of the aforementioned geophysical observation indicates the existence of two belts of middle-to-lower crustal flow around our study area. The high-seismic velocity region in the central part of the Chuan–Dian Block is located between two low-seismic velocity regions, which is consistent with the distribution of the ELIP.

(2) The seismic images also show that the Yangbi area has an obvious boundary of low and high velocity within the depth of 5–15 km, which is NW–SE-trending and extends to the southeast with the depth. This is consistent with the distribution of aftershock sequences of the Yangbi earthquake and the trend of the WX-QHF zone, indicating that the seismogenesis of the Yangbi earthquake might be related to the regional tectonic stress. Meanwhile, the observed low-velocity anomalies are widespread around the northern RRF, east of the Yangbi area, which was expressed as the lower crustal flow, indicating that the stress continues to be transferred southward along the RRF. The soft materials in the middle and lower crust would drag the upper brittle crust and lead to sinistral strike-slip earthquakes.

Data availability statement

The original contributions presented in the study are included in the article/Supplementary Materials; further inquiries can be directed to the corresponding author.

Author contributions

All authors participated in editing and reviewing the manuscript. YS implemented the methodology and writing—original draft preparation. SD implemented related experiments, earthquake relocation, and tomography. JH was involved in data curation and measuring earthquake relocation. All authors contributed to the article and approved the submitted version.

Technology. Some figures were prepared using the public domain Generic Mapping Tools (GMT).

Conflict of interest

The authors declare that the research was conducted in the absence of any commercial or financial relationships that could be construed as a potential conflict of interest.

Publisher's note

All claims expressed in this article are solely those of the authors and do not necessarily represent those of their affiliated organizations, or those of the publisher, the editors, and the reviewers. Any product that may be evaluated in this article, or claim that may be made by its manufacturer, is not guaranteed or endorsed by the publisher.

References

Aki, K., and Lee, W. H. K. (1976). Determination of three-dimensional velocity anomalies under a seismic array using first P arrival times from local earthquakes: 1. A homogeneous initial model. *J. Geophys. Res.* 81 (23), 4381–4399. doi:10.1029/JB081i023p04381

Bai, D., Unsworth, M. J., Meju, M. A., Ma, X., Teng, J., Kong, X., et al. (2010). Crustal deformation of the eastern Tibetan plateau revealed by magnetotelluric imaging. *Nat. Geosci.* 3 (5), 358–362. doi:10.1038/ngeo830

Bao, X., Song, X., Eaton, D. W., Xu, Y., and Chen, H. (2020). Episodic lithospheric deformation in eastern Tibet inferred from seismic anisotropy. *Geophys. Res. Lett.* 47 (3), e2019GL085721. doi:10.1029/2019GL085721

Bao, X., Sun, X., Xu, M., Eaton, D. W., Song, X., Wang, L., et al. (2015). Two crustal low-velocity channels beneath SE Tibet revealed by joint inversion of Rayleigh wave dispersion and receiver functions. *Earth Planet. Sci. Lett.* 415, 16–24. doi:10.1016/j.epsl.2015.01.020

Chen, S., Gao, R., Lu, Z., Zhang, X., Li, W., Liang, Y., et al. (2022). Shallow shear wave velocity structure of the Dongshan sag area using surface wave data in a deep reflection profile of the Yuanmou area of Yunnan province, China. *Tectonophysics* 843, 229606. doi:10.1016/j.tecto.2022.229606

Cheng, J., Xu, X. W., Gan, W. J., Ma, W. T., Chen, W. T., and Zhang, Y. (2012). Block model and dynamic implication from the earthquake activities and crustal motion in the southeastern margin of the Tibetan Plateau. *Chin. J. Geophys.* 55 (4), 1198–1212. doi:10.6038/j.issn.0001-5733.2012.04.016

Clark, M. K., and Royden, L. H. (2000). Topographic ooze: Building the eastern margin of Tibet by lower crustal flow. *Geology* 28 (8), 703–706. doi:10.1130/0091-7613(2000)028<0703:tobtem>2.3.co;2

Dai, A., Tang, C. C., Liu, L., and Xu, R. (2020). Seismic attenuation tomography in southwestern China: Insight into the evolution of crustal flow in the Tibetan Plateau. *Tectonophysics* 792, 228589. doi:10.1016/j.tecto.2020.228589

Deng, S., Zhang, W., Yu, X., Song, Q., and Wang, X. (2020). Analysis on crustal structure characteristics of southern Sichuan-Yunnan by regional double-difference seismic tomography. *Chin. J. Geophys.* 63 (10), 3653–3668. doi:10.6038/cjg2020N0383

Hansen, B. E. (1992). Testing for parameter instability in linear models. *J. policy Model.* 14 (4), 517–533. doi:10.1016/0161-8938(92)90019-9

He, B., Xu, Y., and Xiao, L. (2003). Formation mechanism and spatial distribution of igneous rocks in Emei Mountain: New evidence from sedimentary stratigraphy[J]. *Acta Geol. Sin.* 2003 (02), 194–202.

Hedlund, B. P., Cole, J. K., Williams, A. J., Hou, W., Zhou, E., Li, W., et al. (2012). A review of the microbiology of the Rehai geothermal field in Tengchong, Yunnan Province, China. *Geosci. Front.* 3 (3), 273–288. doi:10.1016/j.gsf.2011.12.006

Hu, J., Zhao, T., and Bai, C. Y. (2021). Three-dimensional P and S wave velocity structure and earthquake relocation of the May 21, 2021 Yangbi source region. *Chin. J. Geophys.* 64 (12), 4488–4509. in Chinese. doi:10.6038/cjg2021P0456

Hu, S., He, L., and Wang, J. (2000). Heat flow in the continental area of China: A new data set. *Earth Planet. Sci. Lett.* 179 (2), 407–419. doi:10.1016/S0012-821X(00)00126-6

Huang, J. L., and Zhao, D. P. (2004). Crustal heterogeneity and seismotectonics of the region around Beijing, China. *Tectonophysics* 385 (1–4), 159–180. doi:10.1016/j.tecto.2004.04.024

Huang, Z., Tilmann, F., Comte, D., and Zhao, D. (2019). PWave azimuthal anisotropic tomography in northern Chile: Insight into deformation in the subduction zone. *J. Geophys. Res. Solid Earth* 124 (1), 742–765. doi:10.1029/2018JB016389

Jin, H., Gao, Y., Su, X., and Fu, G. (2019). Contemporary crustal tectonic movement in the southern Sichuan-Yunnan block based on dense GPS observation data. *Earth Planet. Phys.* 3 (1), 53–61. doi:10.26464/epp2019006

Kong, W., Huang, L., Yao, R., and Yang, S. (2022). Contemporary kinematics along the Xianshuihe-Xiaojiang fault system: Insights from numerical simulation. *Tectonophysics* 839, 229545. doi:10.1016/j.tecto.2022.229545

Lei, J., and Zhao, D. (2009). Structural heterogeneity of the Longmenshan fault zone and the mechanism of the 2008 Wenchuan earthquake (Ms 8.0). *Geochem. Geophys. Geosystems* 10 (10), 002590. doi:10.1029/2009GC002590

Li, C., Shan, X., Zhang, G., Zhao, C., Gong, W., and Zhang, Y. (2022). Slip kinematics of the 2021 Yangbi earthquake: Fore-Main-Aftershock sequence rupture along an unknown secondary fault of the weixi–qiaohou fault. *Seismol. Res. Lett.* 93 (3), 1400–1412. doi:10.1785/0220210220

Li, Y., Wu, Q., Zhang, R., Tian, X., and Zeng, R. (2008). The crust and upper mantle structure beneath Yunnan from joint inversion of receiver functions and Rayleigh wave dispersion data. *Phys. Earth Planet. Inter.* 170, 134–146. doi:10.1016/j.pepi.2008.08.006

Liu, C., Yao, H., Yang, H. Y., Shen, W., Fang, H., Hu, S., et al. (2019). Direct inversion for three-dimensional shear wave speed azimuthal anisotropy based on surface wave ray tracing: Methodology and application to Yunnan, southwest China. *J. Geophys. Res. Solid Earth* 124 (11), 11394–11413. doi:10.1029/2018JB016920

Liu, J., Zhang, L., and Du, Y. (2020). Seismic hazard assessment of the mid-northern segment of Xiaojiang fault zone in southwestern China using scenario earthquakes. *Bull. Seismol. Soc. Am.* 110 (3), 1191–1210. doi:10.1785/0120190248

Liu, Y., Li, L., van Wijk, J., Li, A., and Fu, Y. V. (2021). Surface-wave tomography of the Emeishan large igneous province (China): Magma storage system, hidden hotspot track, and its impact on the Capitanian mass extinction. *Geology* 49 (9), 1032–1037. doi:10.1130/G49055.1

Long, F., Qi, Y., Yi, G., Wu, W., Wang, G., Zhao, X., et al. (2021). Relocation of the M S 6.4 Yangbi earthquake sequence on May 21, 2021 in Yunnan Province and its seismogenic structure analysis. *Chin. J. Geophys.* 64 (8), 2631–2646. doi:10.6038/cjg2021O0526

Lu, H., Feng, G., He, L., Liu, J., Gao, H., Wang, Y., et al. (2022). An improved source model of the 2021 M w 6.1 Yangbi earthquake (southwest China) based on InSAR and BOI datasets. *Remote Sens.* 14 (19), 4804. doi:10.3390/rs14194804

Lun, L., Chen, C., Yuanyuan, F., and Hongjian, F. (2023). Multiple surface wave tomography methods and their applications to the Tibetan Plateau. *Rev. Geophys. Planet. Phys.* 54 (2), 174–196. doi:10.19975/j.dqyxx.2022-019

Lv, M., Ding, Z., and Xu, X. (2022). Seismogenic environments of earthquakes on the southeastern margin of the Tibetan Plateau revealed by double-difference tomography. *Tectonophysics* 843, 229603. doi:10.1016/j.tecto.2022.229603

Ma, X., McElhinny, M. W., Embleton, B. J., and Zhang, Z. (1993). Permo-Triassic palaeomagnetism in the Emei mountain region, southwest China. *Geophys. J. Int.* 114 (2), 293–303. doi:10.1111/j.1365-246x.1993.tb03918.x

Mooney, W. D., Ritsema, J., and Hwang, Y. K. (2012). Crustal seismicity and the earthquake catalog maximum moment magnitude (Mcmax) in stable continental regions (SCRs): Correlation with the seismic velocity of the lithosphere. *Earth Planet. Sci. Lett.* 357, 78–83. doi:10.1016/j.epsl.2012.08.032

Rawlinson, N., Pozgay, S., and Fishwick, S. (2010). Seismic tomography: A window into deep Earth. *Phys. Earth Planet. Interiors* 178 (3-4), 101–135. doi:10.1016/j.pepi.2009.10.002

Royden, L. H., Burchfiel, B. C., King, R. W., Wang, E., Chen, Z., Shen, F., et al. (1997). Surface deformation and lower crustal flow in eastern Tibet. *science* 276 (5313), 788–790. doi:10.1126/science.276.5313.788

Sun, Q., Guo, Z., Pei, S., Fu, Y. V., and Chen, Y. J. (2022). Fluids triggered the 2021 Mw 6.1 Yangbi earthquake at an unmapped fault: Implications for the tectonics at the northern end of the Red River fault. *Seismol. Res. Lett.* 93 (2A), 666–679. doi:10.1785/0220210227

Sun, X., Bao, X., Xu, M., Eaton, D. W., Song, X., Wang, L., et al. (2014). Crustal structure beneath SE Tibet from joint analysis of receiver functions and Rayleigh wave dispersion. *Geophys. Res. Lett.* 41, 1479–1484. doi:10.1002/2014gl059269

Sun, Y., Niu, F., Liu, H., Chen, Y., and Liu, J. (2012). Crustal structure and deformation of the SE Tibetan plateau revealed by receiver function data. *Earth Planet. Sci. Lett.* 349, 186–197. doi:10.1016/j.epsl.2012.07.007

Tapponnier, P., and Molnar, P. (1976). Slip-line field theory and large-scale continental tectonics. *Nature* 264 (5584), 319–324. doi:10.1038/264319a0

Tapponnier, P., Peltzer, G. L. D. A. Y., Le Dain, A. Y., Armijo, R., and Cobbold, P. (1982). Propagating extrusion tectonics in Asia: New insights from simple experiments with plasticine. *Geology* 10 (12), 611–616. doi:10.1130/0091-7613(1982)10<611: petian>2.0.co;2

Waldhauser, F., and Ellsworth, W. L. (2000). A double-difference earthquake location algorithm: Method and application to the northern Hayward fault, California. *Bull. Seismol. Soc. Am.* 90, 1353–1368. doi:10.1785/0120000006

Waldhauser, F. (2001). hypoDD-A program to compute double-difference hypocenter locations. doi:10.7916/D8SN072H

Wang, E., and Burchfiel, B. C. (2000). Late Cenozoic to Holocene deformation in southwestern Sichuan and adjacent Yunnan, China, and its role in formation of the southeastern part of the Tibetan Plateau. *Geol. Soc. Am. Bull.* 112 (3), 413–423. doi:10.1130/0016-7606(2000)112<413:lcthdi>2.0.co;2

Wang, F., Shi, W., Zhang, W., Wu, L., Yang, L., Wang, Y., et al. (2017). Differential growth of the northern Tibetan margin: Evidence for oblique stepwise rise of the Tibetan Plateau. *Sci. Rep.* 7 (1), 41164–41169. doi:10.1038/srep41164

Wang, Y., Hu, S., He, X., Guo, K., Xie, M., Deng, S., et al. (2021). Relocation and focal mechanism solutions of the 21 May 2021 M S 6.4 Yunnan Yangbi earthquake sequence. *Chin. J. Geophys.* 64 (12), 4510–4525. doi:10.6038/cjg2021P0401

Wei, L., Qingju, W., Fengxue, Z., Sun, L. Y., Zeng, Z. G., Qu, W., et al. (2019). A new approach to accomplish intraoperative cholangiography in left lateral segmentectomy of living liver donation. *Acta Seismol. Sin.* 41 (2), 155–161. doi:10.12659/AOT.915400

Wei, W., Zhao, D., and Xu, J. (2013). P-wave anisotropic tomography in Southeast Tibet: New insight into the lower crustal flow and seismotectonics. *Phys. Earth Planet. Interiors* 222, 47–57. doi:10.1016/j.pepi.2013.07.002

Xie, Z., Zheng, Y., Liu, C., Xiong, X., Li, Y., and Zheng, X. (2015). Source parameters of the 2014 Ms 6.5 Ludian earthquake sequence and their implications on the seismogenic structure. *Seismol. Res. Lett.* 86 (6), 1614–1621. doi:10.1785/0220150085

Xin, H., Zhang, H., Kang, M., He, R., Gao, L., and Gao, J. (2019). High-resolution lithospheric velocity structure of continental China by double-difference seismic travel-time tomography. *Seismol. Res. Lett.* 90 (1), 229–241. doi:10.1785/0220180209

Xu, Y., and Zhong, S. (2001). Emei Mountain igneous rocky province: Evidence of mantle plume activity and its melting conditions[J]. *Geochemistry* 2001 (01), 1–9. doi:10.19700/j.0379-1726.2001.01.002

Xu, Y., Yang, X. T., and Liu, J. H. (2013). Tomographic study of crustal velocity structures in the Yunnan region southwest China. *Chin. J. Geophys.* 56 (6), 1904–1914. doi:10.6038/cjg20130613

Yang, W., Ding, Z., Liu, J., Cheng, J., Zhang, X., Wu, P., et al. (2021). Velocity structure of the northeastern end of the Bayan Har block, China, and the seismogenic environment of the Jiuzhaigou and Songpan-Pingwu earthquakes: Inferences from double-difference tomography. *Bull. Seismol. Soc. Am.* 111 (4), 2195–2208. doi:10.1785/0120200224

Yang, Y., Yao, H. J., Wu, H. X., Zhang, P., and Wang, M. M. (2020). A new crustal shear-velocity model in Southwest China from joint seismological inversion and its implications for regional crustal dynamics. *Geophys. J. Int.* 220, 1379–1393. doi:10.1093/gji/ggz514

Yao, H., van Der Hilst, R. D., and De Hoop, M. V. (2006). Surface-wave array tomography in SE Tibet from ambient seismic noise and two-station analysis—I. Phase velocity maps. *Geophys. J. Int.* 166 (2), 732–744. doi:10.1111/j.1365-246X.2006.03028.x

Yao, H., van der Hilst, R. D., and Montagner, J. P. (2010). Heterogeneity and anisotropy of the lithosphere of SE Tibet from surface wave array tomography. *J. Geophys. Res. Solid Earth* 115 (B12), B12307. doi:10.1029/2009JB007142

Zhang, H., and Thurber, C. H. (2003). Double-difference tomography: The method and its application to the Hayward fault, California. *Bull. Seismol. Soc. Am.* 93 (5), 1875–1889. doi:10.1785/0120020190

Zhang, P. Z., Shen, Z., Wang, M., Gan, W., Burgmann, R., Molnar, P., et al. (2004). Continuous deformation of the Tibetan Plateau from global positioning system data. *Geology* 32 (9), 809–812. doi:10.1130/G20554.1

Zhang, Y., An, Y., Long, F., Zhu, G., Qin, M., Zhong, Y., et al. (2022). Short-term foreshock and aftershock patterns of the 2021 Ms 6.4 Yangbi earthquake sequence. *Seismol. Res. Lett.* 93 (1), 21–32. doi:10.1785/0220210154

Zhang, Y., Meng, Q., Wang, Z., Lu, X., and Hu, D. (2021). Temperature variations in multiple air layers before the mw 6.2 2014 ludian earthquake, yunnan, China. *Remote Sens.* 13 (5), 884. doi:10.3390/rs13050884

Zhang, Z., Yao, H., and Yang, Y. (2020). Shear wave velocity structure of the crust and upper mantle in Southeastern Tibet and its geodynamic implications. *Sci. China Earth Sci.* 63, 1278–1293. doi:10.1007/s11430-020-9625-3

Zhao, D., Hasegawa, A., and Horiuchi, S. (1992). Tomographic imaging of P and S wave velocity structure beneath northeastern Japan. *J. Geophys. Res. Solid Earth* 97 (B13), 19909–19928. doi:10.1029/92JB00603

Zheng, X. F., Yao, Z. X., Liang, J. H., and Zheng, J. (2010). The role played and opportunities provided by IGP DMC of China National Seismic Network in Wenchuan earthquake disaster relief and researches. *Bull. Seismol. Soc. Am.* 100 (5B), 2866–2872. doi:10.1785/0120090257

Zhou, L. Q., Liu, J., Su, Y. J., Ma, H. S., and Zhou, J. (2009). Tomography for Q of Yunnan region from high-frequency attenuation of S wave. *Chin. J. Geophys.* 52 (6), 1500–1507. doi:10.3969/j.issn.0001-5733.2009.06.011